

Multifractal analysis of the fracture surfaces of foamed polypropylene/polyethylene blends

Chuang Liu^{a,b}, Xiu-Lei Jiang^c, Tao Liu^c, Ling Zhao^c, Wei-Xing Zhou^{a,b,d,e,*}, Wei-Kang Yuan^c

^aSchool of Business, East China University of Science and Technology, Shanghai 200237, China

^bResearch Center of Systems Engineering, East China University of Science and Technology, Shanghai 200237, China

^cState Key Laboratory of Chemical Engineering, East China University of Science and Technology, Shanghai 200237, China

^dSchool of Science, East China University of Science and Technology, Shanghai 200237, China

^eResearch Center for Econophysics, East China University of Science and Technology, Shanghai 200237, China

Abstract

The two-dimensional multifractal detrended fluctuation analysis is applied to reveal the multifractal properties of the fracture surfaces of foamed polypropylene/polyethylene blends at different temperatures. Nice power-law scaling relationship between the detrended fluctuation function F_q and the scale s is observed for different orders q and the scaling exponent $h(q)$ is found to be a nonlinear function of q , confirming the presence of multifractality in the fracture surfaces. The multifractal spectra $f(\alpha)$ are obtained numerically through Legendre transform. The shape of the multifractal spectrum of singularities can be well captured by the width of spectrum $\Delta\alpha$ and the difference of dimension Δf . With the increase of the PE content, the fracture surface becomes more irregular and complex, as is manifested by the facts that $\Delta\alpha$ increases and Δf decreases from positive to negative. A qualitative interpretation is provided based on the foaming process.

Key words: Fracture surface; batch foaming; multifractal detrended fluctuation analysis; singularity spectrum; complexity

1. Introduction

The plastic foam industry is fast growing and the plastic foams have drawn a great deal of interest in recent decades [1]. The cell sizes of the plastic foams strongly influence the application of the materials [2]. The microcellular polymer, with cell sizes hundreds of times smaller than those of conventional plastic foams, can offer some unique properties that conventional foams do not possess, such as higher impact strength, higher toughness, higher stiffness-to-weight ratio, higher fatigue life, higher thermal stability, lower dielectric constant, and lower thermal conductivity [3, 4, 5, 6]. Therefore, microcellular polymer has wide industrial and everyday-life applications including food packaging, airplane and automotive parts, sporting equipment, insulation, controlled release devices and filters, and so on [7, 8]. The sizes and morphology of cells have considerable influence on the application of foaming materials, which are usually studied using the fracture surfaces

[9, 10, 11, 12, 13, 14].

In most cases, fracture surfaces of different materials are self-similar, which can be characterized by fractal and multifractal theories [15]. The monofractal properties of the morphology of fracture surfaces have been investigated for metals [16, 17], ceramics [18, 19, 20], polymers [21, 22, 23, 24], concretes [25, 26, 27, 28], alloys [29, 30, 31, 32, 33, 34], rocks [35, 36, 37, 38, 39], and many other materials. Moreover, the multifractal features of surfaces have also been studied. Raoufi *et al.* analyzed the multifractal spectrum of ITO thin films prepared by electron beam deposition method and the $f(\alpha)$ shapes of ITO thin films remained left hooked after annealing at 200°C and 300°C [40]. Moktadir *et al.* researched the multifractal properties of Pyrex and silicon surfaces blasted with sharp particles, and found that the long-range correlations were the origin of the multifractal behaviour [41].

In this work, we investigate the multifractal properties of the fracture surfaces of polypropylene (PP) and polyethylene (PE) blends foamed with supercritical carbon dioxide. The two-dimensional multifractal detrended fluctuation analysis (MF-DFA) is adopted, which has the advantages of easy implementation, high precision, and low computational time [42]. The MF-DFA approach has been applied to investigate the landscape of the Yardangs region on Mars and the fracture sur-

* Corresponding author. Address: 130 Meilong Road, P.O. Box 114, East China University of Science and Technology, Shanghai 200237, China, Phone: +86 21 64253634, Fax: +86 21 64253152.

Email addresses: liutao@ecust.edu.cn (Tao Liu), wzzhou@ecust.edu.cn (Wei-Xing Zhou).

Nomenclature

s	scale of boxes
$X(i, j)$	two-dimensional matrix
$u_{v,w}(i, j)$	cumulative sum
$\tilde{u}_{v,w}(i, j)$	fitting bivariate polynomial
$\epsilon_{v,w}(i, j)$	residual matrix
q	order of detrended fluctuation function
$F_q(s)$	detrended fluctuation function
D_f	fractal dimension
$h(q)$	scaling exponent function
$\tau(q)$	mass exponent function
$\alpha(q)$	singularity strength function
α_{\max}	maximum singularity
α_{\min}	minimum singularity
$\Delta\alpha$	width of multifractal spectrum
$f(\alpha)$	multifractal singularity spectrum
Δf	difference, $\Delta f = f(\alpha_{\max}) - f(\alpha_{\min})$
T	foaming temperature
w	weight fraction of PE
P	probability measure

face of a foamed polyurethane sample with supercritical carbon dioxide [42], the combustion flames in four-burner impinging entrained-flow gasifier [43] and Pollocks's drip paintings [44].

2. Experimental

2.1. Materials

The isotactic polypropylene (Y1600) we have used was purchased from Shanghai Petrochemical Company, China. The crystallinity and melting temperature of the isotactic polypropylene was 47% and 169°C, respectively.

The low density polyethylene (2426H) was purchased from Yangzi Petrochemical Company, China. The crystallinity and melting temperature of the low density polyethylene was 42% and 111.2°C, respectively.

The CO₂ (purity: 99.9%) supplied by Shanghai Air Product Company, China, was utilized as a blowing agent.

2.2. Experiment process

Five different weight fractions of the PP/PE blends were studied, in which the PP fractions are 100%, 95%, 90%, 75% and 50%. The blends were prepared in a Haake Minilab system, which is based on a conical twin-screw compounder with

an integrated backflow channel. The blending was carried out for 10 minutes under a 0.6 MPa nitrogen atmosphere with a blending temperature of 190°C and a screw speed of 50 rounds per minute. After blending, the rod-like PP/PE blends were collected at the die exit for foaming.

Fig. 1 illustrates the schematic experimental setup of the depressurization batch foaming process. A high-pressure vessel in stainless steel was used. The internal volume of the vessel was 80 cm³, calibrated with distilled water by a syringe pump. A pressure transducer of type P31 from Beijing Endress & Hauser Ripenss Instrumentation Company Limited, was used to measure the pressure with a precision of ±0.01 MPa and a valve of type Swagelok SS-1RS8MM to release the CO₂ gas. A computer installed with a PCI bus data acquisition system was connected to the above pressure transducer to record the pressure decay during a depressurization process.

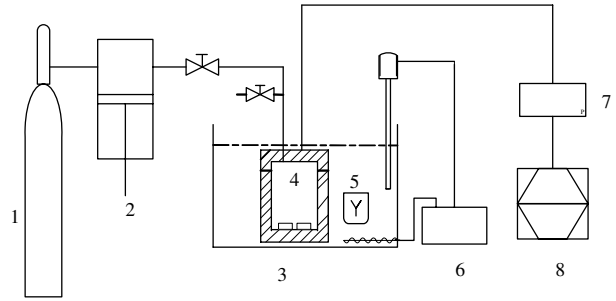


Fig. 1. Schematic diagram of the experiment setup for the batch foaming process: 1, CO₂ steel cylinder; 2, syringe pump; 3, oil bath; 4, high-pressure vessel; 5, stirrer; 6, temperature controller; 7, pressure transducer; 8, data acquisition system.

In the foaming process, all PP/PE blends samples (including the pure PP sample for comparison) were placed in the high-pressure vessel to ensure the same foaming condition and the vessel was purged with low-pressure CO₂. Thereafter, a given amount of CO₂ was charged. The CO₂ loading was achieved by a DZB-1A syringe pump of Beijing Satellite Instrument Company (China) with a precision of 0.01 cm³. The high-pressure vessel was immersed in a silicone oil bath and rapidly heated to a desired saturation temperature. After the sorption of CO₂ into the blends samples reached a sort of equilibrium, the CO₂ was released rapidly from the high-pressure vessel. The foamed blends samples were taken out for subsequent analysis. The samples were immersed in liquid nitrogen for 10 minutes and then fractured. The cell morphologies of the foamed blends samples were characterized by a JSM-6360LV scanning electron microscopy (SEM). The polymer foaming was influenced by many factors. In this work, we consider the influence of different mixture ratios at two different temperature $T = 150$ and 140°C.

2.3. SEM images

From the experiments, many SEM pictures of the fracture surface of the foams under different experimental conditions were obtained. Fig. 2 illustrates a typical image of fracture surface of the foamed sample prepared at 150°C and 25 MPa with

a depressurization rate of 200 MPa/s and the mixture ratio PP : PE = 90 : 10. The depressurization rate was not a constant during the depressurization process. The rate of 200 MPa/s was the largest depressurization rate during the whole depressurization process, which is the key parameter mainly determining the cell nucleation rate. The data acquisition system obtained the change of pressure with time and then we were able to calculate the depressurization rate at any time, such that the depressurization rate can be calculated as the ratio of the pressure difference over the depressurization time. The size of the images was 960×1280 pixels, and we intercepted them into 800×1200 to eliminate the noise of the mark on the images. The images were stored in the computer as two-dimensional arrays in 256 grey levels for multifractal analysis.

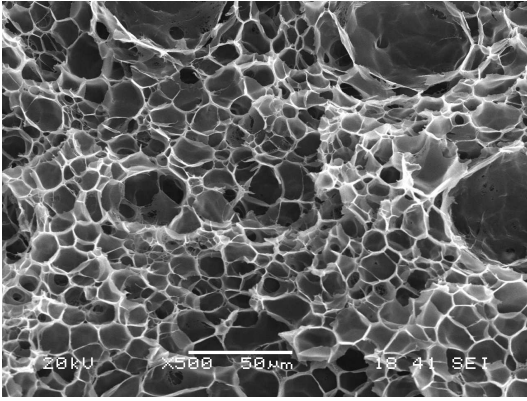


Fig. 2. SEM micrograph of the foamed sample (PP : PE = 90 : 10) under condition: 150°C, 25 MPa, depressurization rate 200 MPa/s.

Fig. 3 illustrates a typical fracture surface image of the foamed sample prepared at 150°C, 25 MPa, with the depressurization rate of 200 MPa/s, and the mixture ratio PP : PE = 50 : 50. And we can find the open-cell easily, and the same result can be obtained at 140°C. Thus, we can imagine that there is a threshold content of PE in the sample at the range 25% ~ 50% where the cells change to open.

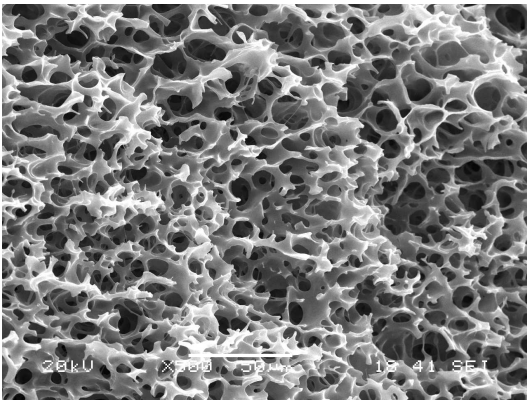


Fig. 3. SEM micrograph of the foamed sample (PP : PE = 50 : 50) under condition: 150°C, 25 MPa, depressurization rate 200 MPa/s.

3. Two-dimensional multifractal detrended fluctuation analysis

The multifractal properties may exist in the fracture surface of the foams. To unveil the multifractal characteristics of the SEM images, the two-dimensional MF-DFA is applied. This method has become popular for its simplicity and easy computer implementation. The two-dimensional MF-DFA is the extension of the DFA method which is frequently used in computing the roughness exponent of monofractal signals and the identification of long range correlations in non-stationary time series [45]. The two-dimensional MF-DFA applied to our experiment data can be summarized as following steps:

Step 1. Consider a self-similar (or self-affine) surface, which is denoted by a two-dimensional array $X(i, j)$, where $i = 1, 2, \dots, M$ and $j = 1, 2, \dots, N$. The surface is partitioned into $M_s \times N_s$ disjoint square segments of the same size $s \times s$, where $M_s = [M/s]$ and $N_s = [N/s]$. Each segment can be denoted by $X_{v,w}$ such that $X_{v,w}(i, j) = X(l_1 + i, l_2 + j)$ for $1 \leq i, j \leq s$, where $l_1 = (v - 1)s$ and $l_2 = (w - 1)s$.

Since M and N are often not a multiple of the segment size s , two orthogonal strips at the end of the profile may remain and some data will be ignored by this way. In order to take these ending parts of the surface into consideration, the same partitioning procedure can be repeated starting from the other three corners. Then there will be $4M_s N_s$ segments and calculating the average over them can eliminate the boundary influence.

Step 2. For each segment $X_{v,w}$ identified by v and w , the cumulative sum $u_{v,w}(i, j)$ is calculated as follows:

$$u_{v,w}(i, j) = \sum_{k_1=1}^i \sum_{k_2=1}^j X_{v,w}(k_1, k_2), \quad (1)$$

where $1 \leq i, j \leq s$. Note that $u_{v,w}$ itself is a surface.

Step 3. The trend of the constructed surface $u_{v,w}$ can be determined by fitting it with a prechosen bivariate polynomial function $\tilde{u}_{v,w}(i, j)$. The parameters of $\tilde{u}_{v,w}(i, j)$ can be estimated easily through the least square method fit to the data in each segment $X_{v,w}$. Then, the residual matrix can be obtained. The detrended fluctuation function $F(v, w, s)$ of the segment $X_{v,w}$ is defined via the sample variance of the residual matrix:

$$F^2(v, w, s) = \frac{1}{s^2} \sum_{i=1}^s \sum_{j=1}^s [u_{v,w}(i, j) - \tilde{u}_{v,w}(i, j)]^2. \quad (2)$$

Step 4. The overall detrended fluctuation is calculated by averaging over all the segments, and the value of the q th-order fluctuation function is

$$F_q(s) = \left\{ \frac{1}{M_s N_s} \sum_{v=1}^{M_s} \sum_{w=1}^{N_s} [F(v, w, s)]^q \right\}^{1/q}, \quad (3)$$

where q can take any real value except for $q = 0$. When $q = 0$, we have

$$F_0(s) = \exp \left\{ \frac{1}{M_s N_s} \sum_{v=1}^{M_s} \sum_{w=1}^{N_s} \ln[F(v, w, s)] \right\} \quad (4)$$

according to L'Hôpital's Rule.

Step 5. Varying the value of s in the range from $s_{\min} \approx 6$ to $s_{\max} \approx \min(M, N)/4$, we can determine the scaling relation between the detrended fluctuation function $F_q(s)$ and the size scale s , which reads:

$$F_q(s) \sim s^{h(q)}, \quad (5)$$

where the exponent $h(q)$ is called the generalized Hurst index. The scaling exponent $h(q)$ is a constant for monofractals and a nonlinear decreasing function of q for multifractals. For positive q values, $h(q)$ describes the scaling behaviour of the segments with large fluctuations, whereas for negative q values $h(q)$ concerns with small fluctuations.

In the standard multifractal formalism based on partition function [46], the multifractal nature is characterized by the mass exponents $\tau(q)$, which is a nonlinear function of q . The $\tau(q)$ function is related to $h(q)$ through

$$\tau(q) = qh(q) - D_f \quad (6)$$

where D_f is the fractal dimension of the geometric support of the multifractal measure [42, 45]. According to the Legendre transform, we can obtain the singularity strength function $\alpha(q)$ and the singularity spectrum $f(\alpha)$ as follows [46]:

$$\alpha = \tau'(q) = h(q) + qh'(q), \quad (7)$$

$$f(\alpha) = q\alpha(q) - \tau(q). \quad (8)$$

4. Results

4.1. Multifractal analysis

As a first step, we perform multifractal analysis on the SEM images to check if the fracture surfaces possess multifractal nature or not. We take the SEM picture showed in Fig. 2 as an example to illustrate the power-law scaling between the detrended fluctuation function $F_q(s)$ and the scale s . Fig. 4 shows the fluctuation $F_q(s)$ as a function of s for five different values of q in double-logarithmic coordinates. The results for $q = -3, 0, 3$ and 6 have been shifted upward by $0.4, 0.8, 1.2$ and 1.6 for clarity. According to the figure, the data points for every q fall on a straight line, indicating a perfect power-law scaling between $F_q(s)$ and s , as expressed in Eq. (5). The scaling range is from 6 pixels to 200 pixels for all q values. The fluctuation functions $F_q(s)$ of other fracture surfaces also exhibit nice power-law behaviors.

According to Eq. (5), the slopes of the straight lines illustrated in Fig. 4 are the scaling exponent $h(q)$, which can be determined by simple linear regressions of $\ln F_q(s)$ against $\ln s$ for different q . Fig. 5 illustrates $h(q)$ as a function of q for $-6 \leq q \leq 6$ with the same image. It is noteworthy to point out that, due to the finite size of the data, the overall fluctuation values $F_q(s)$ for too large q are not statistically significant. It is evident that $h(q)$ is a decreasing nonlinear function of q . The mass exponent function $\tau(q)$ is also calculated numerically using Eq. (6), where $D_f = 2$. The inset of Fig. 5 shows the mass exponent function $\tau(q)$ for $-6 \leq q \leq 6$. The nonlinearity of

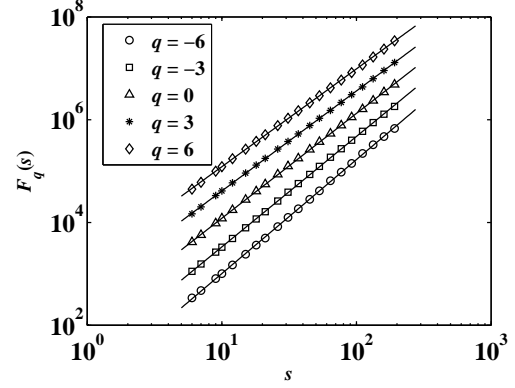


Fig. 4. Log-log plots of $F_q(s)$ versus s for five different values of q . The lines are the best power-law fits to the data. The plots for $q = -3, 0, 3$ and 6 are shifted upward by $0.4, 0.8, 1.2$ and 1.6 for clarity.

$h(q)$ and $\tau(q)$ confirms that the fracture surface under investigation possesses multifractal nature. We note that all other fracture surfaces also exhibit multifractality.

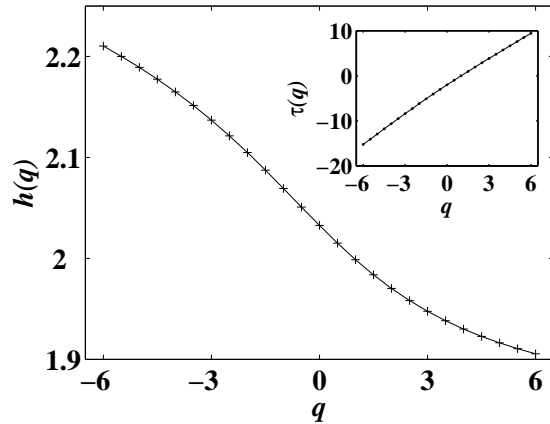


Fig. 5. Dependence of the scaling exponent $h(q)$ with respect to the order q . The inset shows the mass exponent function $\tau(q)$.

4.2. Multifractal spectra

Theoretically, the geometric support of a multifractal measure can be decomposed into interwoven fractal sets, each of which is characterized by its singularity strength α . The fractal dimension of the underlying fractal set associated with α is $f(\alpha)$, which is the well-known singularity spectrum or multifractal spectrum. In this vein, α and $f(\alpha)$ are two most important characteristics in the description of the multifractal.

We have numerically obtained the values of $\alpha(q)$ and $f(\alpha)$ through the Legendre transform from $\tau(q)$ for all the fracture surfaces under investigation. Fig. 6 illustrates the multifractal spectra $f(\alpha)$ with respect to α for five samples with different ratios for PP and PE at 150°C . The multifractal spectra for different blends samples exhibit different shapes. With the increase of the proportion of polyethylene, the singularity spectrum becomes wider. It means that the surface with higher polyethylene proportion is more irregular, as is clear from the compar-

ison between Fig. 2 and Fig. 3. Another intriguing feature in Fig. 6 is that the $f(\alpha)$ function for PP = 50% becomes negative when α is larger than about 2.6. The negative dimension ($f(\alpha) < 0$) was investigated in several experiments such as the diffusion-limited aggregation [47] and the energy dissipation field of turbulent flows [48]. The negative dimension describes the rarely occurring events [49] and one needs an exponentially increasing number of samples to observe the subsets with the same α value [48].

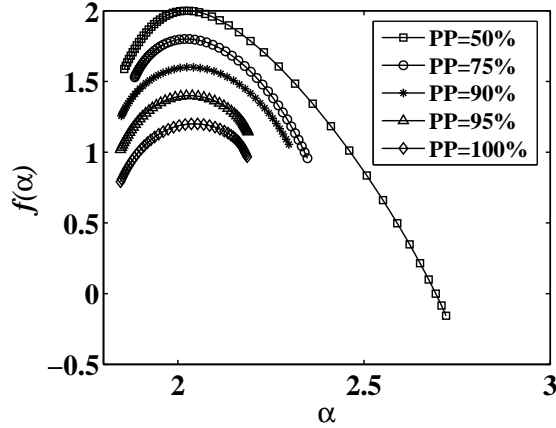


Fig. 6. Multifractal spectra of the fracture surfaces of different PP/PE samples prepared at $T = 150^\circ\text{C}$. The curves for PP = 75%, 90%, 95%, and 100% have been shifted downward by 0.2, 0.4, 0.6 and 0.8 for clarity.

Fig. 7 plots the multifractal spectra $f(\alpha)$ of the singularity α for five samples with different PP/PE ratios at temperature $T = 140^\circ\text{C}$. Again, the multifractal spectra for different blends samples exhibit different shapes and the singularity spectrum becomes wider with the increase of the proportion of polyethylene. However, no negative dimension is observed in this case.

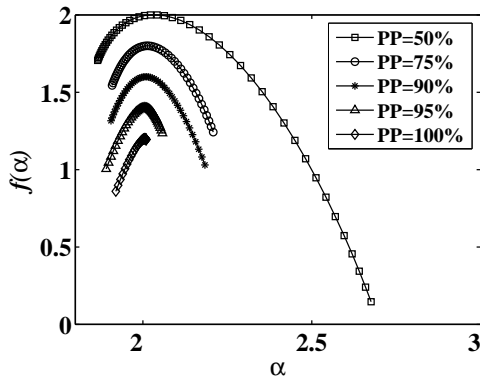


Fig. 7. Multifractal spectra of the fracture surfaces of different PP/PE samples prepared at $T = 140^\circ\text{C}$. The curves for PP = 75%, 90%, 95%, and 100% have been shifted downward by 0.2, 0.4, 0.6 and 0.8 for clarity.

5. Discussion

There are several fundamental quantities related to the multifractal spectrum. The minimum and maximum singularities

α_{\min} and α_{\max} are the singularity strengths associated with the regions of the sets where the measures are the least and most singular, respectively. The corresponding $f(\alpha_{\min})$ and $f(\alpha_{\max})$ values reflect the fractal dimensions of the two regions characterized by $\alpha = \alpha_{\min}$ and $\alpha = \alpha_{\max}$. The shape of the multifractal spectrum $f(\alpha)$ can be captured to a great extent by the width of the multifractal spectrum $\Delta\alpha = \alpha_{\max} - \alpha_{\min}$ and the difference of the fractal dimensions $\Delta f = f(\alpha_{\max}) - f(\alpha_{\min})$. We discuss the dependence of $\Delta\alpha$ and Δf with respect to the PP/PE ratio.

5.1. The dependence of $\Delta\alpha$ with respect to the PP/PE ratio

In the formalism of multifractal, α_{\min} is related to the maximum probability measure by $P_{\max} \sim \varepsilon^{\alpha_{\min}}$, where ε represents the scale approaching zero and it is a small quantity, whereas α_{\max} is related to the minimum probability measure through $P_{\min} \sim \varepsilon^{\alpha_{\max}}$. The width $\Delta\alpha$ can be used to describe the range of the probability measures:

$$P_{\max}/P_{\min} \sim \varepsilon^{-\Delta\alpha}. \quad (9)$$

The greater the $\Delta\alpha$ value, the wider the probability distribution and the larger the foamed growth probability of the surface.

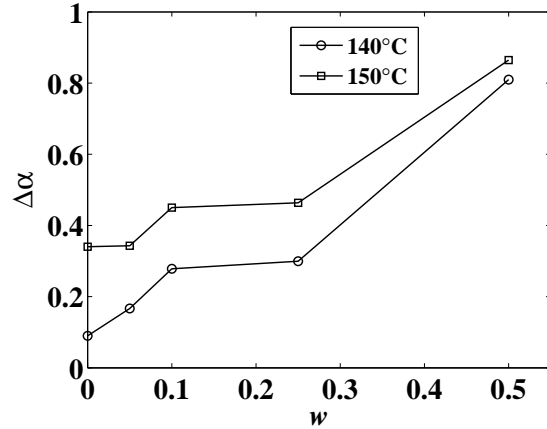


Fig. 8. The width of spectrum $\Delta\alpha$ versus the content of PE (w) for two temperatures.

Fig. 8 illustrates the relationship between $\Delta\alpha$ and the content of PE in the sample at two different temperatures. We find that the value of $\Delta\alpha$ increases with augmenting PE accretion. This well agrees with the experimental results that the number of cells in the sample increases with the increase of the PE content, and the fracture surface becomes more irregular. We also find that the two curves at different temperaments share almost the same variation tendency. Since PP is a semicrystalline polymer with a high crystallinity degree, it needs a very rigorous condition for PP foaming since gases do not dissolve in the crystalline regions [50, 51, 52]. According to Fig. 8, the $\Delta\alpha$ value of the pure PP sample is merely 0.089, which means that the fracture surfaces of pure PP samples are close to monofractal. When PE is added in the sample, the PE with a low crystallization temperature (T_c) can be molten (the melting

point of LDPE we used is 111.2°C) in 140°C, and both the cell nucleation and bubble growth may take place in the region of the molten PE. Therefore, mixing with PE makes the sample foaming easier, and we obtain wider multifractal spectra with the increase of the PE content while the crystalline regions may remain intact. Comparing the two curves in Fig. 8, the curve for foaming at $T = 150^\circ\text{C}$ is above that of $T = 140^\circ\text{C}$, which is consistent with the results that higher temperatures cause larger foamed regions with more cells and larger cell size [53].

According to Fig. 8, $\Delta\alpha$ increases very quickly when the content of PE is more than 25%. The cell opening may be the reason for this transient phenomenon. In our experiment, the soft sections (PE) form minor and dispersed phases and the hard sections (PP) form a major melt matrix. Cell opening can be initiated and propagated through well-dispersed soft domains that are entrapped between growing adjacent cells. Even though these soft domains can become elongated as cells grow (i.e., cell walls become thinner), cell opening is most likely to be initiated at the weakest cell wall sections because of the embedded soft polymer phases [52]. When the content of PE reaches a certain value, the cell may be opening and continuous to form a three-dimensional network, which leads to a much wider distribution of the singularity of the fracture surface. We can observe easily the open cells in Fig. 3 at $T = 150^\circ\text{C}$, and at $T = 140^\circ\text{C}$ as well.

5.2. The dependence of Δf with respect to the PP/PE ratio

The parameter Δf is also a very important quantity in the multifractal analysis. The $f(\alpha_{\max})$ value reflects the fractal dimension of the subset of the minimum growth probability with $N_{P_{\min}} = N_{\alpha_{\max}} \sim \varepsilon^{-f(\alpha_{\max})}$, while $f(\alpha_{\min})$ reflects that of the maximum probability such that $N_{P_{\max}} = N_{\alpha_{\min}} \sim \varepsilon^{-f(\alpha_{\min})}$. Hence, the $\Delta f(\alpha)$ value can describe the ratio between the regions that the probability measure distributes most concentrated and most rarified

$$N_{P_{\max}}/N_{P_{\min}} \sim \varepsilon^{\Delta f}. \quad (10)$$

Thus, $\Delta f < 0$ means that there are more concentrated regions than rarified sites, whereas $\Delta f > 0$ means the contrary.

Fig. 9 depicts the dependence of Δf with respect to the content of PE in the sample at two different temperatures. With the increase of the PE content, the Δf value changes from positive to negative, which reflects the change of multifractal spectrum shape from left-hooked to right-hooked as showed in Fig. 6 and Fig. 7. It implies that the fracture surface becomes more complex and singular when there are more PE in the sample.

The observed multifractal behaviour can be partly interpreted in terms of the spatial intermittency [54, 55] and the origin of the multifractal hidden in the fracture surface may be the long range correlations of the intermittent fluctuation [41, 56]. A basic foaming process can be divided into three steps [4]: (1) mixing, formation of a homogeneous solution composed of foaming agent and polymer melt; (2) cell nucleation, phase separation induced by a thermodynamic instability which is usually a

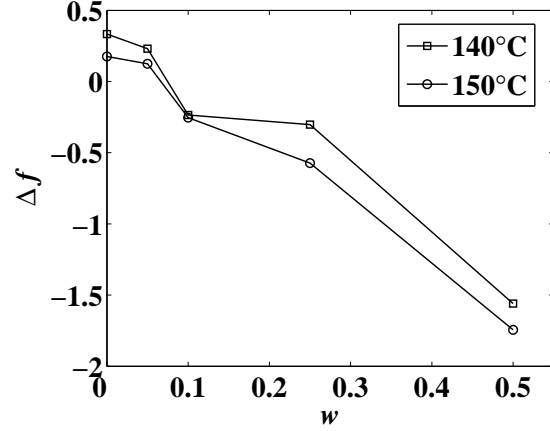


Fig. 9. The difference of fractal dimension Δf versus the content of PE (w) for two temperatures.

temperature increase or a pressure decrease; (3) cell growth and coalescence, a combination of mass transfer and fluid dynamics. In bubble growth and coalescence, the gas (CO_2) transferred from small bubble (with high pressure) to big bubble (with low pressure) to form the foamed structure [57, 58], which may be the origin of long-range correlation. However, in-depth mechanism (mass transfer and fluid dynamics) research of foaming is needed to support this surmise.

6. Conclusion

Foaming is a very complex process, and it is a challenging task to underpin the exact mechanism explaining the nucleation and bubble growth [57]. In this work, we obtained the foamed mixed polymers by batch foaming at fixed pressure and depressurization rate. We used the two-dimensional multifractal detrended fluctuation analysis to unveil the multifractal properties of the fracture surfaces of formed PP/PE blends samples. Perfect power-law scaling is observed and nonlinear relationship between the scaling exponent $h(q)$ and q in the considering moment order $-6 \leq q \leq 6$ show that the fracture surface exhibits multifractal nature.

The two important multifractal parameters $\Delta\alpha$ and Δf were calculated to describe the multifractal nature of the fracture surfaces. We have found that, with the increase of the PE fraction, the fracture surfaces become more and more irregular and complex, which is indicated by the facts that $\Delta\alpha$ increases and Δf decreases. These two parameters can serve as “complexity measures” of the fracture surfaces of foamed polymer blends, and other surfaces as well.

Acknowledgments:

We are grateful to Zhi-Qiang Jiang and Gao-Feng Gu for discussions. This work was partly supported by the National Basic Research Program of China (No. 2004CB217703), the National Natural Science Foundation of China (Grant No. 50703011), the Program for Changjiang Scholars and Innovative Research Team in University (IRT0620), the Program for New Century Excellent Talents in University (NCET-07-

0288), the NSFC/PetroChina through a major joint project on multiscale methodology (No. 20490200), and the Project Sponsored by the Scientific Research Foundation for the Returned Overseas Chinese Scholars, State Education Ministry.

References

- [1] L. J. Lee, C.-C. Zeng, X. Cao, X.-M. Han, J. Shen, G.-J. Xu, Polymer nanocomposite foams, *Compos. Sci. Technol.* 65 (2005) 2344–2363.
- [2] H.-L. Sun, J. E. Mark, S.-C. Tan, N. Venkatasubramanian, M. D. Houtz, F. E. Arnold, C. Y. C. Lee, Microcellular foams from some high-performance composites, *Polymer* 46 (2005) 6623–6632.
- [3] S. P. Nalawade, F. Picchioni, L. P. Janssen, Supercritical carbon dioxide as a green solvent for processing polymer melts: Processing aspects and applications, *Prog. Polym. Sci.* 31 (2006) 19–43.
- [4] D. L. Tomasko, H.-B. Li, D.-H. Liu, X.-M. Han, M. J. Wingert, L. J. Lee, A review of CO₂ applications in the processing of polymers, *Ind. Eng. Chem. Res.* 42 (2003) 6431–6456.
- [5] D. I. Collias, D. G. Baird, R. J. Borggreve, Impact toughening of polycarbonate by microcellular foaming, *Polymer* 35 (1994) 3978–3983.
- [6] V. Kumar, Microcellular polymers: Novel materials for the 21st century, *Cell. Polym.* 12 (1993) 207–223.
- [7] K. W. Suh, C. P. Park, M. J. Maurer, M. H. Tusim, R. D. Genova, P. S. Daniel, Lightweight cellular plastics, *Adv. Mater.* 12 (2000) 1779–1789.
- [8] K. Krause, H. J. P. Sijbesma, P. Mönöklü, N. F. A. van der Vegt, M. Wessling, Bicontinuous nanoporous polymers by carbon dioxide foaming, *Macromolecules* 34 (2001) 8792–8801.
- [9] C. B. Park, Processing and characterization of microcellular foamed high-density polyethylene/isotactic polypropylene blends, *Polym. Eng. Sci.* 38 (1998) 1205–1215.
- [10] A. Chandra, S.-Q. Gong, L.-S. Turng, Cell development in microcellular injection molded Polyamide-6 nanocomposit and neat resin, *J. Cell. Plast.* 40 (2004) 371–382.
- [11] B. Krause, K. Diekmann, N. F. A. van der Vegt, M. Wessling, Open nanoporous morphologies from polymeric blends by carbon dioxide foaming, *Macromolecules* 35 (2002) 1738–1745.
- [12] W.-T. Zhai, J. Yu, L.-C. Wu, W.-M. Ma, J.-S. He, Heterogeneous nucleation uniformizing cell size distribution in microcellular nanocomposites foams, *Polymer* 47 (2006) 7580–7589.
- [13] A. M. Kraynik, D. A. Reinelt, F. van Swol, Structure of random foam, *Phys. Rev. Lett.* 93 (2004) 208301.
- [14] S. Hilgenfeldt, A. M. Kraynik, D. A. Reinelt, J. M. Sullivan, The structure of foam cells: Isotropic plateau polyhedra, *Europhys. Lett.* 67 (2004) 484–490.
- [15] B. B. Mandelbrot, *The Fractal Geometry of Nature*, W. H. Freeman, New York, 1983.
- [16] B. B. Mandelbrot, D. E. Passoja, A. J. Paullay, Fractal character of fracture surfaces of metals, *Nature* 308 (1984) 721–722.
- [17] U. Wendt, K. Stiebe-Lange, M. Smid, On the influence of imaging conditions and algorithms on the quantification of surface topography, *J. Microscopy* 207 (2002) 169–179.
- [18] J. J. J. Mecholsky, D. E. Passoja, K. S. Feinberg-Ringel, Quantitative analysis of brittle fracture surfaces using fractal geometry, *J. Am. Ceram. Soc.* 72 (1989) 60–65.
- [19] J. Y. Thompson, K. J. Anusavice, B. Balasubramaniam, J. J. J. Mecholsky, Effect of microcracking on the fracture toughness and fracture surface fractal dimension of lithia-based glass-ceramics, *J. Am. Ceram. Soc.* 78 (1995) 3045–3049.
- [20] A. Celli, A. Tucci, L. Esposito, P. Carlo, Fractal analysis of cracks in alumina-zirconia composites, *J. Euro. Ceram. Soc.* 23 (2003) 469–479.
- [21] C. T. Chen, J. Runt, Fractal analysis of polystyrene fracture surfaces, *Polym. Commun.* 30 (1989) 334.
- [22] J. Yu, T. Xu, Y. Tian, X. Chen, Z. Luo, The effects of the aggregation structure parameters on impact-fractured surface fractal dimension and strain-energy release rate for polypropylene, *Materials and Design* 23 (2002) 89–95.
- [23] F. Lapique, P. Meakin, J. Feder, T. Jøssang, Self-affine fractal scaling in fracture surfaces generated in ethylene and propylene polymers and copolymers, *J. Appl. Polym. Sci.* 86 (2002) 973–983.
- [24] W.-X. Zhou, B. Li, T. Liu, G.-P. Cao, L. Zhao, W.-K. Yuan, Shape complexity and fractality of fracture surfaces of swelled isotactic polypropylene with supercritical carbon dioxide, *Phys. Rev. E* 73 (2006) 011801.
- [25] L. Dougan, P. Addison, Estimating the cut-off in the fractal scaling of fractured concrete, *Com. Concr. Res.* 31 (2001) 1043–1048.
- [26] Y. Wang, S. Diamond, A fractal study of the fracture surfaces of cement pastes and mortars using a stereoscopic sem method, *Com. Concr. Res.* 31 (2001) 1385–1392.
- [27] M. A. Issa, M. A. Issa, M. S. Islam, A. Chudnovsky, Fractal dimension - A measure of fracture roughness and toughness of concrete, *Eur. Financ. Management* 70 (2003) 125–137.
- [28] A. Yan, K.-R. Wu, D. Zhang, W. Yao, Influence of concrete composition on the characterization of fracture surface, *Cem. Concr. Comp.* 25 (2003) 153–157.
- [29] E. Bouchaud, G. Lapasset, J. Planés, Fractal dimension of fractured surfaces - A universal value, *Europhys. Lett.* 13 (1990) 73–79.
- [30] C. H. Shek, G. M. Lin, K. L. Lee, J. K. L. Lai, Fractal fracture of amorphous fe46ni32v2si14b6 alloy, *J. Non-Crystalline Solids* 224 (1998) 244–248.
- [31] X. Wang, H. Zhou, Z. Wang, M. Tian, Y. Liu, Q. Kong, Fractal analysis of cyclic creep fractured surfaces of two high temperature alloys, *Materials Sci. Engin. A* 266 (1999) 250–254.
- [32] V. I. Betekhtin, P. N. Butenko, V. L. Gilyarov, V. E. Korsukov, A. S. Luk'yanenko, B. A. Obidov, V. E. Khartsiev, The effect of uniaxial tension on the relief geometry of

- the surface of an $\text{Fe}_{77}\text{Ni}_{19}\text{Si}_9\text{B}_3$ amorphous alloy, *Tech. Phys. Lett.* 28 (2002) 26–29.
- [33] F. Paun, E. Bouchaud, Morphology of damage cavities in aluminium alloys, *Int. J. Fracture* 121 (2003) 43–54.
- [34] A. Eftekhari, Fractal study of ni-cr-mo alloy for dental applications: effect of beryllium, *Appl. Surface Sci.* 220 (2003) 343–348.
- [35] J. Schmittbuhl, F. Schmitt, C. Scholz, Scaling invariance of crack surfaces, *J. Geophys. Res. B* 100 (1995) 5953–5974.
- [36] J. M. López, J. Schmittbuhl, Anomalous scaling of fracture surfaces, *Phys. Rev. E* 57 (1998) 6405–6408.
- [37] H. Xie, H. Sun, Y. Ju, Z. Feng, Study on generation of rock fracture surfaces by using fractal interpolation, *Int. J. Solids Struct.* 38 (2001) 5765–5787.
- [38] T. Babadagli, K. Develi, Fractal characteristics of rocks fractured under tension, *Theor. Appl. Fracture Mech.* 39 (2003) 73–88.
- [39] H. W. Zhou, H. Xie, Direct estimation of the fractal dimensions of a fracture surface of rock, *Surface Rev. Lett.* 10 (2003) 751–762.
- [40] D. Raoufi, H. R. Fallah, A. Kiasatpour, A. S. Rozatian, Multifractal analysis of ITO thin films prepared by electron beam deposition method, *Appl. Surface Sci.* 254 (2008) 2168–2173.
- [41] Z. Moktadir, M. Kraft, H. Wensink, Multifractal properties of pyrex and silicon surfaces blasted with sharp particles, *Physica A* 387 (2008) 2083–2090.
- [42] G.-F. Gu, W.-X. Zhou, Detrended fluctuation analysis for fractals and multifractals in higher dimensions, *Phys. Rev. E* 74 (2006) 061104.
- [43] M.-R. Niu, W.-X. Zhou, Z.-Y. Yan, Q.-H. Guo, Q.-F. Liang, F.-C. Wang, Z.-H. Yu, Multifractal detrended fluctuation analysis of combustion flames in four-burner impinging entrained-flow gasifier, *Chem. Engn. J.* (2008) in press.
- [44] J. Alvarez-Ramirez, C. Lbarra-Valdez, E. Rodriguez, L. Dagdug, $1/f$ -Noise structures in Pollocks’s drip paintings, *Physica A* 387 (2008) 281–295.
- [45] J. W. Kantelhardt, S. A. Zschiegner, E. Koscielny-Bunde, S. Havlin, A. Bunde, H. E. Stanley, Multifractal detrended fluctuation analysis of nonstationary time series, *Physica A* 316 (2002) 87–114.
- [46] T. C. Halsey, M. H. Jensen, L. P. Kadanoff, I. Procaccia, B. I. Shraiman, Fractal measures and their singularities: The characterization of strange sets, *Phys. Rev. A* 33 (1986) 1141–1151.
- [47] C. Amitrano, A. Coniglio, F. di Liberto, Growth probability distribution in kinetic aggregation processes, *Phys. Rev. Lett.* 57 (1986) 1016–1019.
- [48] A. B. Chhabra, K. R. Sreenivasan, Negative dimensions: Theory, computation and experiment, *Phys. Rev. A* 43 (1991) 1114–1117.
- [49] B. B. Mandelbrot, Negative fractal dimensions and multifractals, *Physica A* 163 (1990) 306–315.
- [50] H. E. Naguib, C. B. Park, N. Reichelt, Fundamental foaming mechanisms governing the volume expansion of extruded polypropylene foams, *J. Appl. Polym. Sci.* 91 (2004) 2661–2668.
- [51] H. E. Naguib, C. B. Park, S.-W. Song, Effect of supercritical gas on crystallization of linear and branched polypropylene resins with foaming additives, *Ind. Eng. Chem. Res.* 44 (2005) 6685–6691.
- [52] C. Patrick, J. Wang, C. B. Park, Extruded open-cell foams using two semicrystalline polymers with different crystallization temperatures, *Ind. Eng. Chem. Res.* 45 (2006) 175–181.
- [53] Z.-M. Xu, X.-L. Jiang, T. Liu, G.-H. Hu, L. Zhao, Z.-N. Zhu, W.-K. Yuan, Foaming of polypropylene with supercritical carbon dioxide, *J. Supercrit. Fluids* 41 (2007) 299–310.
- [54] F. Argoul, A. Arneodo, G. Grasseau, Y. Gagne, E. J. Hopeinger, U. Frisch, Wavelet analysis of turbulence reveals the multifractal nature of the Richardson cascade, *Nature* 338 (1989) 51–53.
- [55] Y. Kuramoto, H. Nakao, Scaling properties in large assemblies of simple dynamical units driven by long wave random forcing, *Phys. Rev. Lett.* 78 (1997) 4039–4042.
- [56] N. Mordant, J. Delour, E. Leveque, A. Arneodo, J. F. Pinton, Long time correlations in lagrangian dynamics: a key to intermittency in turbulence, *Phys. Rev. Lett.* 89 (2002) 254502.
- [57] S. N. Leung, C. B. Park, D.-L. Xu, H.-B. Li, R. G. Fenton, Computer simulation of bubble-growth phenomena in foaming, *Ind. Eng. Chem. Res.* 45 (2006) 7826–7831.
- [58] S. N. Leung, H.-B. Li, C. B. Park, Impact of approximating the initial bubble pressure on cell nucleation in polymeric foaming, *J. Appl. Polym. Sci.* 104 (2007) 902–908.